

DEVELOPMENT OF A CFD MODEL AND METHODOLOGY FOR THE INTERNAL FLOW SIMULATION IN A HYDROGEN-POWERED UAV

Alessandro Porcarelli  ¹

¹Department of Engineering Mechanics, KTH Royal Institute of Technology, Stockholm, Sweden

Abstract

The onboard carrying of a hydrogen fuel cell leads to unexplored internal flow characteristics, including the introduction of water vapour. Given the strict environmental operational requirements of PEM fuel cells, a Runge-Kutta-based solver is developed and tested to effectively and efficiently assess the evolution of the UAV internal bay flow temperature and humidity fields.

Keywords: CFD, UAV, Hydrogen Fuel Cells, Internal Flow, Runge-Kutta Projection Method

1. Introduction

Within the last decade, civil applications of UAVs are expanding their horizons, particularly in the surveillance field. A growth of the UAV industry is following from this development. The most promising solution to achieve the long endurance requirement of UAV-operated surveillance missions is combining batteries and hydrogen fuel cells in a hybrid propulsion system. On one hand, the high specific energy provided by hydrogen fuel cells allows to reach a large flight endurance [1]. On the other hand, the batteries cope with the limited specific power of fuel cells, providing additional power during critical flight phases such as take-off and manoeuvres [2]. Polymer Electrolyte Membrane (PEM) fuel cells have been identified as the most convenient choice for long-endurance UAVs [1, 2]. The main advantage of PEMFCs is represented by their low operating temperatures, along with their long life cycle, their ability to withstand large pressure differentials and their limited noise and vibrations [1].

In PEM fuel cells, water is the only output of the reaction and is expelled from the interior part of the device in vapour state. Following the fuel cell chemical reaction, and given the hydrogen and water molar masses, the total mass of water vapour exhausted in the UAV bay can be roughly estimated to account for nine-to-ten times the hydrogen fuel "burnt" by the fuel cell. Clearly, a flying vehicle with a landing weight above the take-off weight would lead to unexplored flight mission managements, and eventual condensation can potentially affect the overall vehicle stability. Moreover, the air in the proximity of the fuel cell intake should be sufficiently cool such that the cathode is always supplied with oxygenated air. Lastly, fuel cells are designed to operate up to a limit ambient temperature. At the same time, the fuel cell exhaust air-stream temperature is generally itself above this limit and contributes to the heating of the internal flow. As the total volume of air inside the UAV's bay is limited, these considerations underline the necessity to equip the vehicle with an intake-exhaust system such that a proper ventilation and water vapour exhaust are ensured.

At the current state of the art in hydrogen fuel cell powered UAVs, there is very limited information regarding intake-exhaust systems. Only few elementary examples have been found in literature where the design is supported by rough calculations or wind tunnel assessments. In Kim et al. [4] and Kim et al. [5], the emphasis is placed on the necessity to cool the fuel cell stack to ensure its performance. Intakes are introduced at the fuselage nose of the glider-shaped UAV, such that abundant air flows through the bay and is exhausted at the rear of the fuselage, taking advantage of the pusher propeller which attracts the flow. While no intake design optimization is documented, a posteriori

wind tunnel tests provided evidence that sufficient air was supplied to cool down the stack. In a similarly glider-shaped UAV, Herwerth et al. [2] and Chiang et al. [3] document a more refined bay flow management. The intakes are positioned in direct proximity of the fuel cell stack, and they are sized in order to provide sufficient cooling and simultaneously limit the introduced airflow and thus the increase of drag. Considering non-hydrogen-powered UAVs, more detailed and complex passive cooling systems are documented. Panagiotou et al. [6] dimension cooling ducts to efficiently supply the payload with properly directed cooling air. The ducts are connected to aerodynamically-efficient NACA-shaped intakes whose preliminary sizing methodology is validated through an internal flow CFD simulation.

The purpose of the present work is to develop a CFD model to simulate the internal flow in a hydrogen fuel cell powered UAV, accounting for both heat transfer and humidity. Given a sample intake-exhaust system, two different numerical approaches considering these two combined flow features will be explored and tested over the blended wing-body UAV geometry being developed at KTH, unit of Aeronautics and Vehicle Engineering [7]. The ultimate goal is to define a model to be applied to perform an optimal design of an intake-exhaust system. The work is an extract of the author's master thesis [8], with the addition of further insights on the validity of the forced convection assumption.

2. Theory

2.1 Governing equations

As the turbulent entities are a defining feature for internal flows, and steady state is not always achieved, an unsteady Reynolds averaged Navier-Stokes (URANS) approach is chosen to achieve a reliable resolved mean flow at a reasonable computational cost. Furthermore, given the low-speed flow, the incompressibility assumption holds. The equations read

$$\frac{\partial U_i}{\partial x_i} = 0; \quad (1a)$$

$$\frac{\partial U_i}{\partial t} + U_j \frac{\partial U_i}{\partial x_j} = -\frac{1}{\rho} \frac{\partial P}{\partial x_i} + \frac{\partial}{\partial x_j} (\nu \frac{\partial U_i}{\partial x_j} - \overline{u'_i u'_j}). \quad (1b)$$

In order to limit the complexity of the model, the gravity term in Equation 1 is neglected. The importance of natural convection resulting from the gravity force with respect to forced convection is defined by the Richardson number

$$Ri = \frac{g \cdot \beta \cdot \Delta T_{max} \cdot L}{U^2}, \quad (2)$$

where g is the gravitational acceleration, β is the thermal expansion coefficient, ΔT_{max} is given by the difference between the maximum flow temperature T_{max} and reference temperature T_{ref} , L is the characteristic length, and U is the characteristic velocity. In order to safely neglect the gravity term, the flow should be dominated by forced convection, i.e. the Richardson number should be kept below 0.1. The occurrence of this condition will be verified in Section 5.

In accordance to the UAV internal flow simulation provided by Panagiotou et al. [6], the two-equations $k - \omega$ SST is selected as the most indicated RANS-based turbulence closure [9]. The model is recognized as the most reasonably general and reliable for a wide class of flows [10].

Given the incompressible flow assumption, the temperature can be solved as a passive scalar, whose behaviour follows a standard advection-diffusion equation, neglecting radiation:

$$\frac{\partial T}{\partial t} + U_i \frac{\partial T}{\partial x_i} = D_T \frac{\partial^2 T}{\partial x_i^2}. \quad (3)$$

The thermal diffusivity of air D_T is assumed to be constant and is given by the sum of a thermodynamic contribution $\alpha = \frac{\lambda}{\rho c_p}$, and a modelled physical turbulent contribution $\alpha_T = \frac{\nu_T}{Pr_T}$, with $Pr_T = 1$.

Considering the humidity field, the flow specific humidity is chosen as the transport variable and it is defined as the weight of water vapor m_v contained in a unit weight of moist air $m_v + m_d$:

$$q = \frac{m_v}{m_v + m_d}, \quad (4)$$

where m_d is the mass of dry air. Following similar assumptions to the temperature field, the specific humidity q is also solved as a passive scalar

$$\frac{\partial q}{\partial t} + U_i \frac{\partial q}{\partial x_i} = D_q \frac{\partial^2 q}{\partial x_i^2}, \quad (5)$$

with its diffusivity D_q found as the sum of a thermodynamic and physical turbulent contribution. To limit the model complexity, a condensation model is not included.

2.2 Numerical solvers

The customized numerical solvers are implemented and tested in OpenFOAM [12]. The choice of the discretization numerical schemes determines the simulation convergence and the accuracy of its results. While higher-order schemes introduce a minor truncation error and are thus more precise, lower-order schemes are more dissipative and prevent instabilities to grow. Open-source solvers like OpenFOAM are particularly sensitive to instabilities.

Even if computationally more expensive, a transient solver is highly recommended for internal flows accounting for heat transfer and other scalars. Hence, two different transient time integration methods are compared. The first method consists of the default implicit-time second-order backward PISO solver with two corrector steps [13]. Pressure and velocity are coupled in each timestep, consisting of one predictor step, where an intermediate velocity is computed using the pressure of the previous timestep, and of a number of corrector steps, where the intermediate and final velocity and pressure are obtained iteratively [14]. As a result of the research of a more efficient solver, the second method consists of a low-dissipative fourth-order explicit Runge-Kutta (RK) projection method published by Vuorinen et al. [14]. Mathematically, RK is considered one of the standard methods to solve transient problems of the form

$$\frac{dU}{dt} = f(t, U). \quad (6)$$

The classical fourth-order RK-method (RK4) consists of the solution U^n progression to U^{n+1} according to the following update sequence:

$$\begin{cases} k_1 = f(t^n, U^n)\Delta t, \\ k_2 = f(t^n + \Delta t/2, U^n + k_1/2)\Delta t, \\ k_3 = f(t^n + \Delta t/2, U^n + k_2/2)\Delta t, \\ k_4 = f(t^n + \Delta t, U^n + k_3)\Delta t, \\ U^{n+1} = U^n + (k_1 + 2k_2 + 2k_3 + k_4)/6, \\ t^{n+1} = t^n + \Delta t. \end{cases} \quad (7)$$

In contrast to the operator splitting and corrector loop in PISO, the new solver employs the projection method to couple pressure and velocity, as is often the case when dealing with explicit integration time methods. The method consists of the projection of the velocity field onto its solenoidal counterpart using the pressure gradient in a single projection step [14]. The final OpenFOAM RK-projection code has been implemented following the algorithm account, development and test provided by Vuorinen et al. [14]. Their study also shows an overall algorithm efficiency increase up to nearly 50% in comparison to PISO, whilst not detecting any significant instability growth due to the higher order of accuracy. Both solvers have been further customized to account for temperature and humidity fields transported as passive scalars.

Considering spatial discretization, particular attention has been given to divergence schemes. After following OpenFOAM guide to perform preliminary comparative simulations [15], the blend Gauss linearUpwind scheme has been selected as it has been shown to be able to provide reasonable and stable results whilst not suppressing the most relevant mean turbulent structures through numerical dissipation.

The CFL (Courant–Friedrichs–Lewy) condition appeared to be the most bounding numerical condition to fulfill in the simulation setup. While a small timestep increases consistently the computational time, a too large timestep value can lead the simulation to divergence.

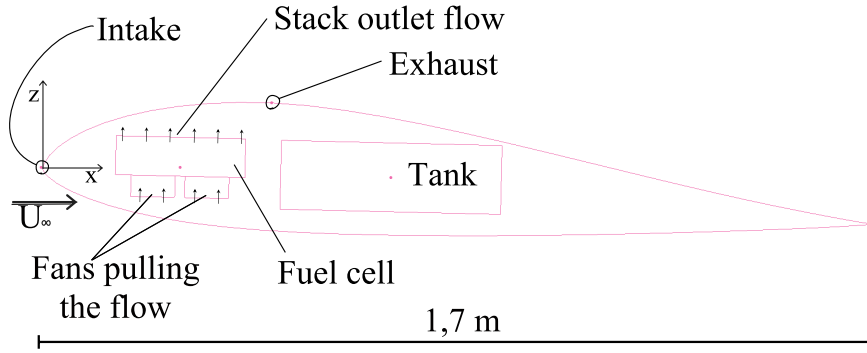


Figure 1 – 2D mid-section of the Green Raven bay.

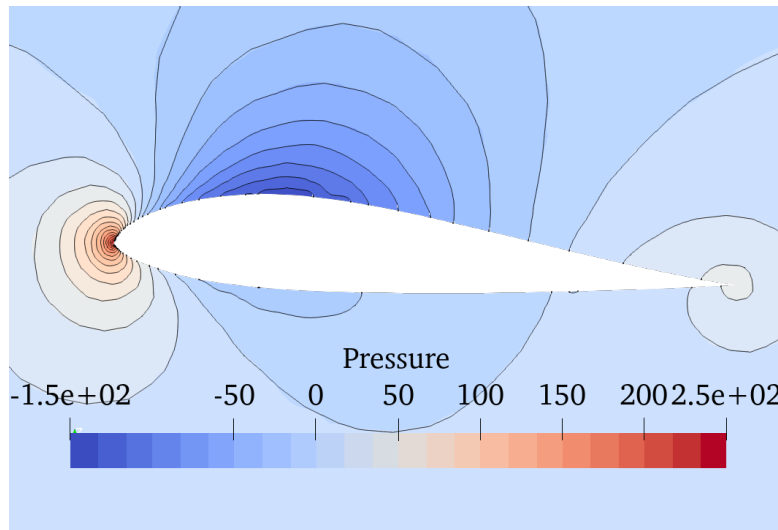


Figure 2 – Contour plot at the mid-cross-section plane computed with a preliminary external flow simulation.

3. CFD setup

In order to properly test the developed CFD model, a realistic sample case should be built. After a careful identification of its desirable features, the 2D mid-cross-section of the Green Raven in Figure 1 has been chosen as the computational domain. A sample intake has been placed at the leading edge close to the external flow stagnation point, and a sample exhaust is located in the upper surface in the proximity of the airfoil maximum thickness. According to preliminary external flow simulations, these two positions are where the higher and lower pressure is experienced by the airfoil, as shown in Figure 2. Hence, the internal flow is expected to take advantage of the consequent blowing and suction effects, respectively.

The design of the near-wall mesh is realized by means of Pointwise® T-rex algorithm, and the outer parent mesh consists of triangles and quadrilaterals which are automatically shaped to comply with high-quality criteria [11]. Furthermore, in order to capture the expected inlet jet-like flow and the outlet confluence flow, a cone-shaped domain fully consisting of quadrilaterals has been designed in correspondence of the intake and the exhaust. Overall, the mesh counts 50k cells. The main mesh features can be observed in Figure 3.

In order to realistically solve the physical problem and achieve simulation convergence, particular attention is given to the definition of the physical boundary conditions. An overview of the geometrical boundary patches is shown in Figure 4. Inlet conditions are defined at the air intake ($U = U_{inf} = 20 \text{ m/s}$), and at the fuel cell stack and fans. In contrast, a pressure condition is set at the exhaust, with the pressure value prescribed at the outlet given by the external flow simulation in its correspondence. Considering the temperature field, $T = T_{ref} = 20 \text{ }^\circ\text{C}$ are assumed at the intake,

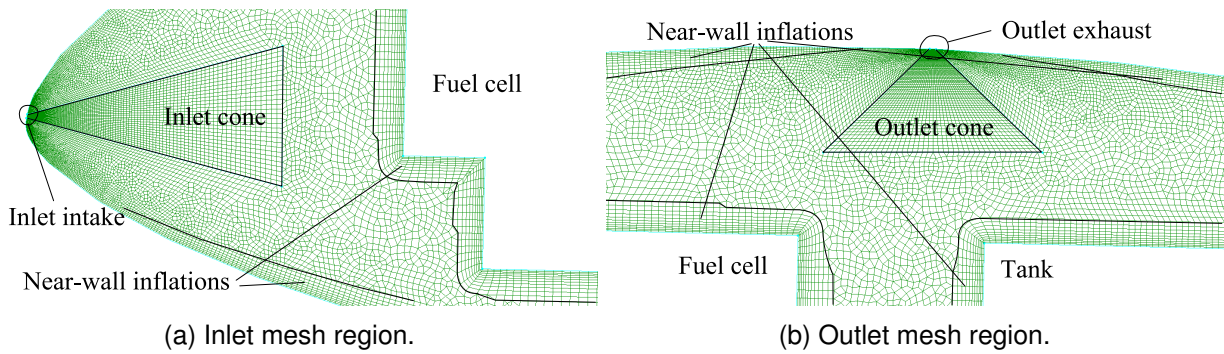


Figure 3 – Mesh design in correspondence of the inlet (3a) and outlet (3b).

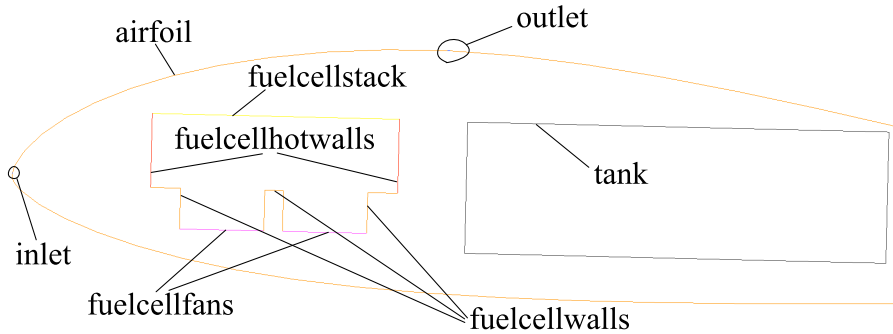


Figure 4 – Outline of the case boundary conditions names.

and the stack temperature of $60\text{ }^{\circ}\text{C}$ is prescribed according to the fuel cell manual [16]. Furthermore, at the fuel cell hot walls a constant heat flux is derived to account for the system heat losses. Finally, a constant specific humidity value is prescribed at the stack, calculated assuming 100% moist air at the stack temperature of $60\text{ }^{\circ}\text{C}$. [8]

The final setup is used to run two comparative simulations employing the PISO solver and the fourth-order Runge-Kutta introduced in Section 2.2.

4. Results

4.1 Quality

In light of the very careful simulation setup, both the RK4 and the PISO simulation converged to low residuals without displaying any instability issue. However, a very small timestep was necessary to fulfill the CFL condition for stability. As a consequence, even if run with domain decomposition and space parallelization, both solvers required a wall clock time of the order of magnitude of days to display appreciable transient flow features. A physical time extension of $t = 10\text{ s}$ proved to be sufficient to achieve relevant results to draw significant conclusions on the validity of the models. In fact, in both cases it was possible to identify a recurrent primary flow pattern across the iterations after a shorter transitory, i.e. well before $t = 10\text{ s}$. An inspection of the velocity field across the time showed that RK4 solution is dominated by mean turbulent swirling motions which do not display any steadiness trend. This was expected given the geometrical complexity of the investigated internal flow, and justifies the choice of a transient numerical solver. In contrast, an overall steady state is achieved with PISO, where the primary flow surrounds the fuel cell in counterclockwise direction (see lower Figure 5 discussed in Section 4.2). This discrepancy can be explained by the higher numerical dissipation performed by the lower-order scheme (second order in time) implemented in PISO, which introduces a larger truncation error and thus tends to suppress the unsteady mean turbulent structures. The achievement of steady state with PISO also explains why the two solvers employ a similar wall clock time even if RK4 is proved to be more efficient [14]. While RK4 iterations are faster in transient and unsteady flow conditions, which are always occurring across the RK4 simulation, PISO iterations speed up once steady state is achieved, thus closing the simulation time gap with RK4.

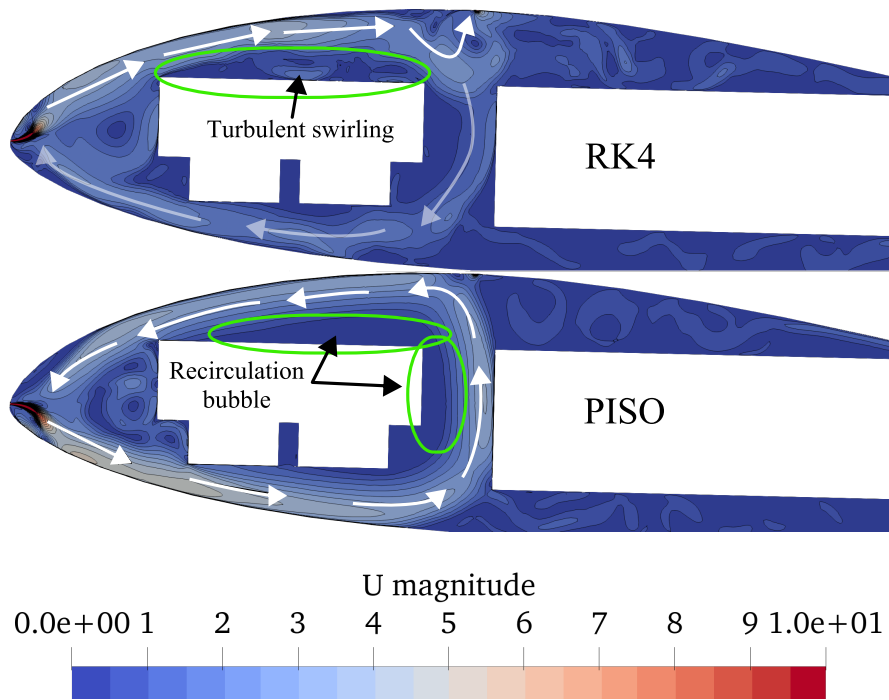


Figure 5 – Contour plot of the velocity field computed with RK4 (upper) and PISO (lower).

A y^+ check is necessary to assess the quality of the near-wall mesh, and ultimately the ability of the setup to capture wall-bounded and separation flow phenomena. The solutions show that the y^+ is kept below 5 in the majority of the domain, i.e. the first near-wall cell fully encloses the viscous sub-layer. This ensures a proper boundary layer flow resolution. Only a negligible region exceeds this threshold in the proximity of the intake.

4.2 Velocity Field

The contour plots of the converged velocity fields at $t = 10s$ computed with RK4 and PISO are shown in upper and lower Figure 5, respectively. In order to better appreciate the velocity gradients at lower speed, and to identify the mean turbulent structures, a same velocity field plot is reported with logarithmic color bar rescaling in Figure 6. It can be immediately observed that the solution differs substantially between the two solvers.

On one hand, RK4 shows that the flow is directed upwards downstream of the inlet, lapping the internal airfoil-shaped upper surface. Hence, the flow diffuses above the fuel cell stack displaying appreciable large-scale mean turbulent structures on top of it. Finally, the primary flow is mostly pulled out of the domain by the low-pressure outlet. The remainder portion of the flow either diffuses further downstream above the tank or travels downwards in the area between the tank and the fuel cell. In the last case, after running in the proximity of the fans, it rejoins the primary flow jet at the intake.

On the other hand, the PISO solution shows a flow which is directed downwards downstream of the inlet. After passing the fuel cell fans, it is pulled by the low-pressure outlet from the bottom to the top. Hence, while only a limited portion is exhausted, most of the flow laps the airfoil-shaped upper surface in the proximity of the stack moving towards the leading edge. An overall steady state is achieved where the primary flow surrounds the fuel cell in a counterclockwise direction. Moreover, the solution field displays a "bubble" of stagnation above the stack and the right hot wall. In RK4, conversely, the flow laps their surfaces with appreciable large-scale unsteady mean turbulent structures.

As introduced in Section 4.1, the reason for this discrepancy probably lies in the higher numerical dissipation performed by the PISO solver, which tends to suppress the mean turbulent structures because of its higher truncation error. According to the theory of discretization schemes and the numerical consistency property, the solution of a lower order scheme should tend to that of a higher

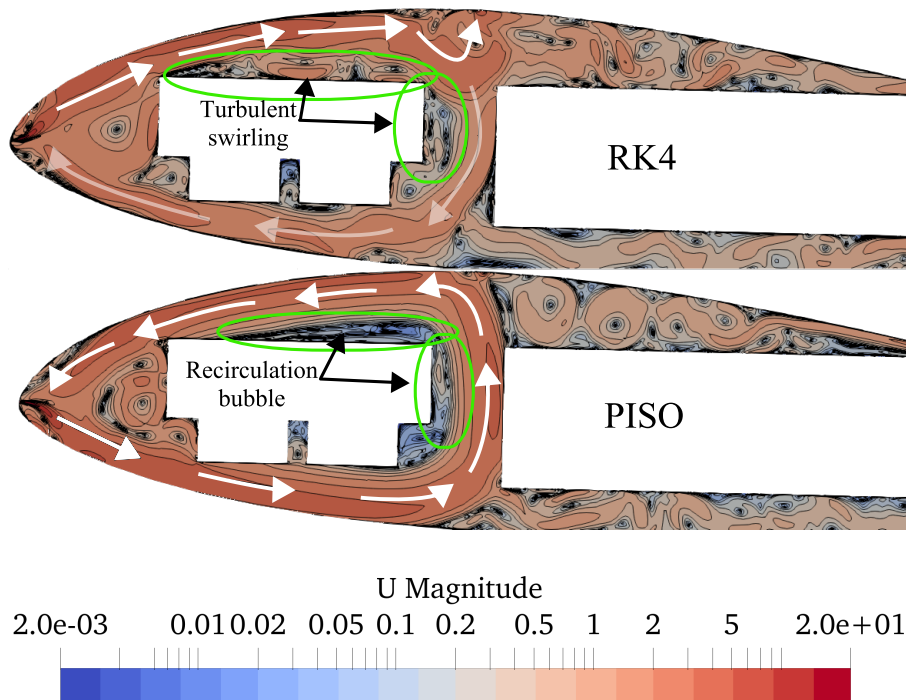


Figure 6 – Logarithmic contour plot of the velocity field computed with RK4 (upper) and PISO (lower).

order one with decreasing timestep Δt and grid element size Δx [17]. Evidently, the fixed Δt and Δx provided in the investigated case fall in a range where substantially different solutions are observed with different order of accuracy schemes. A further mesh refinement and lower timestep would allow the PISO solver to achieve a similar (unsteady) solution to that of RK4. However, this would increase substantially the simulation time, considering also the lower efficiency per iteration of the PISO solver in transient flow conditions. In contrast, the RK4 solver provides a more accurate solution with reasonable setup Δt and Δx and a higher solver efficiency per iteration simultaneously.

4.3 Temperature field

The contour plot of the converged temperature field within the domain is shown in Figure 7. At first glance, it is immediately clear that in the PISO solution an overall more consistent flow heating is observed. In fact, the flow counterclockwise circulation around the fuel cell creates a closed pattern where the air increases its temperature progressively in time under the influence of the fuel cell hot walls and stack. Furthermore, the bubbles of stagnation observed in the velocity field of the PISO solution result in very high-temperature zones in their correspondence, particularly in the proximity of the right fuel cell hot wall. In fact, in a stagnant flow there is a very limited contribution of the convection term in the scalar transport equation, resulting in a consistent local temperature increase. In contrast, as discussed in Section 4.2, the RK4 solution shows a more open flow circulation, with a consistent portion of the flow that is conveyed towards the outlet and exhausted out of the domain. This results in a more efficient overall domain cooling. Furthermore, the mean turbulent structures developed in this higher-accuracy solution around the fuel cell and observed in upper Figure 6 prevent the formation of high temperature bubbles, as proved in the upper Figure 7. The presence of these structures allows to sufficiently locally enhance the convection term contribution in the temperature transport equation to contrast the temperature increase as a consequence of the boundary heat flux and of the boundary high temperature at the stack.

These results point out the substantial importance of an accurate computation of the mean turbulent structures in the model solution in order to correctly predict the temperature transport and evaluate the internal flow cooling and ventilation pattern. As hinted in Section 4.2, with the current setup, only the RK4 higher-order solver is able to efficiently fulfill this requirement.

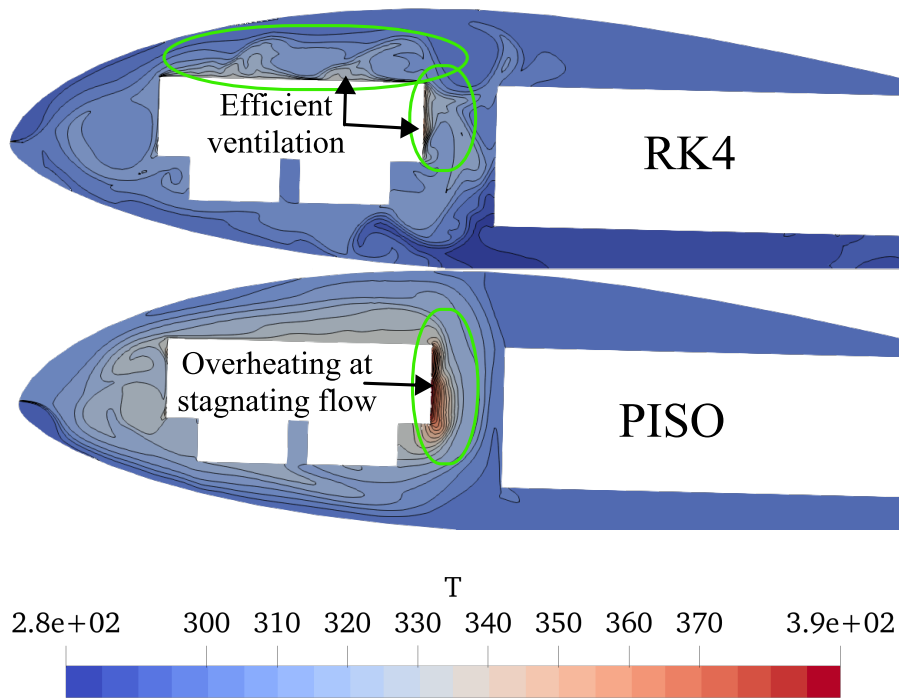


Figure 7 – Contour plot of the temperature field computed with RK4 (upper) and PISO (lower).

4.4 Humidity field

The contour plot of the converged humidity field within the domain is shown in Figure 8. Similarly to the temperature field, it is immediately visible that PISO's lack of resolved mean turbulent structures and close re-circulation flow pattern lead to a consistent humidity stagnation around the fuel cell up to the airfoil-shaped walls. In addition, in correspondence of the bubble of low speed above the stack, a region of higher water vapour concentration is observed. The high flow resident time as a consequence of the re-circulation pattern and the local flow stagnation in the proximity of walls establish favourable conditions for condensation, which is not modelled in the solver.

Considering the solution of RK4, in contrast, the high vapour concentration region near the stack is much more restricted, and the humidity drops moving away from its patch. In fact, the high-momentum primary flow invests the stack with its turbulent structures and entrains the water vapour, which is mostly transported towards the outlet and exhausted as a result of a more open circulation pattern. Hence, the computed scalar concentration around the fuel cell is much more limited indicating an overall more efficient ventilation. In addition, comparing the T and q fields computed by RK4 (upper Figures 7 and 8), a very close similarity in their distribution is observed, particularly on the top of the stack. This analogy indicates that the diffusivity of the two scalars is very similar, with its main contribution given by the turbulent diffusivity.

Once again, these considerations remark the turbulence influence on the scalar transport and underline the importance of the accurate resolution of the mean turbulent structures to achieve reliable scalar solutions. Such resolution is ensured only by the higher-order RK4 solver with the current setup.

Furthermore, the established flow pattern in the RK4 solution suggests that the resident time of the water vapour particles inside the domain is short. Hence, the favourable conditions for water vapour condensation that have been highlighted in the PISO solution are not experienced. This observation raises confidence on the assumed negligible importance of a condensation model whenever an efficient ventilation pattern is established.

5. Forced convection assumption

As introduced in Section 2.1, the necessary condition for neglecting safely the gravity term in the momentum equation is that the flow regime should fall in the forced convection range, i.e. $Ri < 0.1$. In

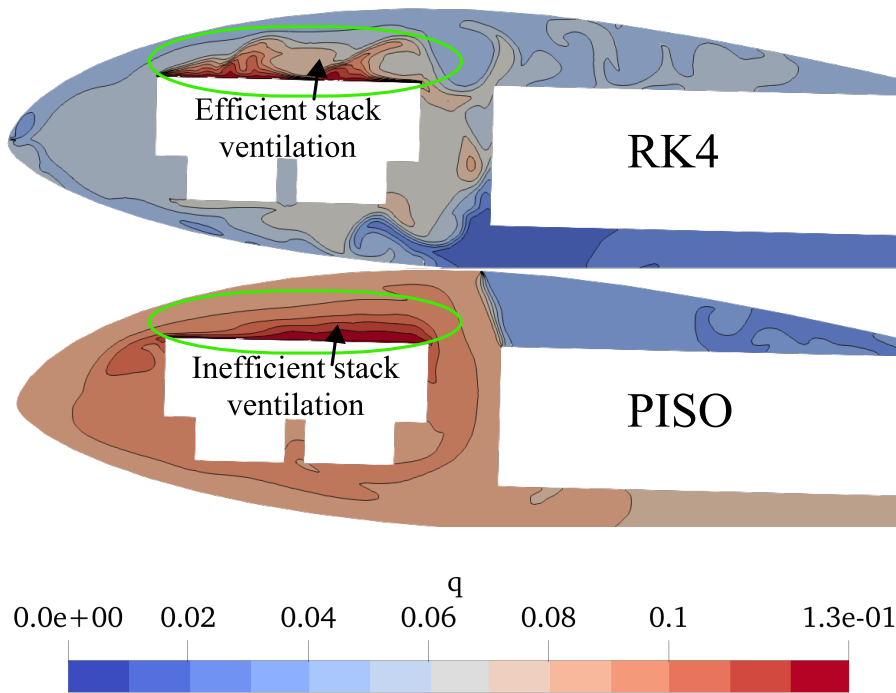


Figure 8 – Contour plot of the specific humidity field computed with RK4 (upper) and PISO (lower).

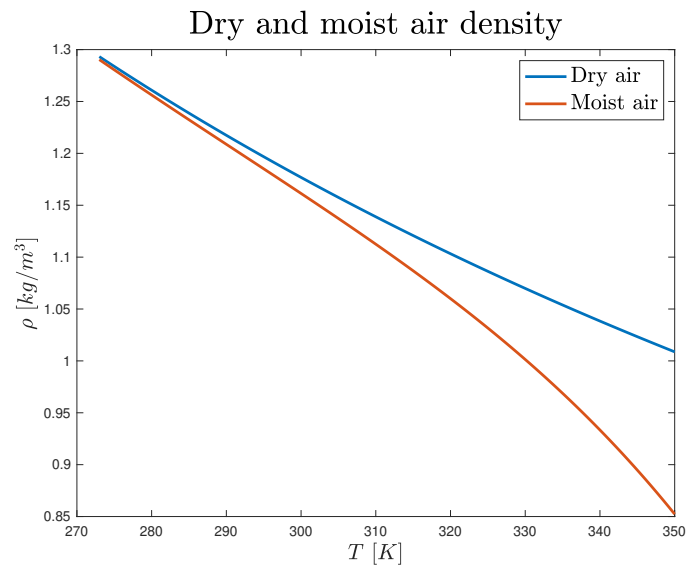


Figure 9 – Comparative plot of the density evolution as a function of temperature for dry and moist air.

this section, the occurrence of this condition is verified with a conservative approach, and a careful choice of each input parameter in Equation 2 is performed.

First of all, the thermal expansion coefficient β is defined as the derivative of the density function with respect to temperature. In Figure 9, $\rho(T)$ is plotted for both dry and moist air. Moist air is evaluated for a relative humidity of 100%, i.e. the maximum allowed content of water vapour per unit dry air. In the investigated setup, this saturation air condition is prescribed at the stack boundary condition. It can be observed that the density curve of moist air is steeper than the one of dry air, particularly as temperature is increased, and this corresponds to an increase of the thermal expansion coefficient in the presence of water vapour and high temperatures. Therefore, the highest and thus most conservative β is experienced at the fuel cell stack, where both maximum water

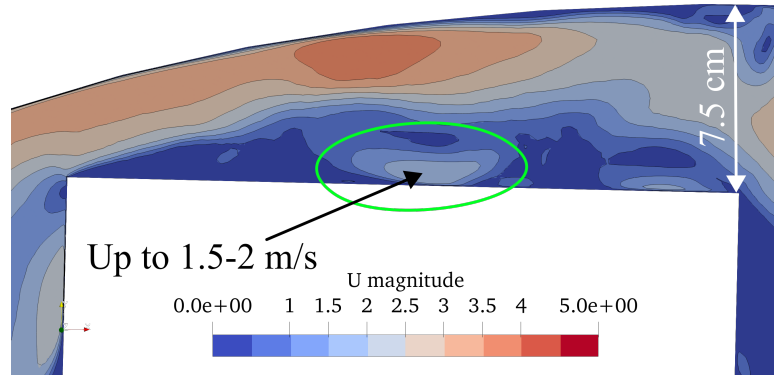


Figure 10 – Local velocity field on top of the fuel cell stack with rescaled color bar range.

vapour concentration and temperature are experienced by the flow. Hence, the thermal expansion coefficient is evaluated for moist air and $T = 60^\circ C$, resulting in $\beta = 6.6 \cdot 10^{-3} \text{ 1/K}$. Similarly, the maximum $\Delta T = T_{max} - T_{ref}$ is experienced at the fuel cell, where $T = T_{max} = 60^\circ C$.

Considering the characteristic length, in a pipe flow case it would be identified as the hydraulic diameter. In the investigated geometrically complex case, it is difficult to quantify this parameter with certainty. As shown in Figure 10, the maximum distance between the fuel cell stack, i.e. the highest temperature and humidity region, and the wall is around 7.5 cm . Therefore, to keep the estimation as conservative as possible, $L = 10 \text{ cm}$ is assumed.

With the discussed conservative input parameters and $g = 9.81 \text{ m/s}^2$, the local flow minimum velocity to fulfill the $Ri < 0.1$ condition is calculated as

$$V_{min} = 1.61 \text{ m/s.} \quad (8)$$

Figure 10 shows the local flow velocity on the top of the fuel cell stack with a rescaled color bar range. In correspondence on the unsteady mean turbulent structures that lap the stack across the physical time and enhance the local scalar transport, the velocity is shown to be in the $1.5 - 2.0 \text{ m/s}$ range. Even if locally lower velocity regions can be identified, the unsteady flow ensures that the whole stack region is crossed by turbulent vortices from time to time. Therefore, considering the more accurate RK4 solution, the flow can be concluded to fall in the forced convection regime and thus the gravity term in the momentum equation can be safely neglected.

6. Conclusions

With the goal of evaluating the internal flow of a hydrogen-powered UAV, where the diffusion of both temperature and water vapour should be taken into account, the performance of two solvers have been evaluated. The higher-order RK4 solver is concluded to provide a more accurate solution with a cheaper setup in terms of timestep and cell element size, and to ensure simultaneously a higher solver efficiency per iteration. The higher order of accuracy of this solver is also shown to be necessary on the tested sample case setup in order to predict the local formation of mean turbulent structures, and consequently to reliably resolve the scalar transport. Furthermore, results have shown that the main assumptions at the basis of the model are verified whenever an efficient internal cooling and ventilation flow pattern is established. Under these conditions, which should be the case in a prospective optimized geometry, non-favourable conditions for condensation and forced convection flow regime are in fact ensured, thus allowing to safely skip the condensation modelling and neglect the gravity term in the momentum equation. Ultimately, it can be concluded that the RK4 solver developed can be employed prospectively for the design of an optimal UAV 3D intake-exhaust system. The only model limitation highlighted in the investigated sample setup is its long computational time, mainly caused by the very small timestep necessary to satisfy the CFL condition. Nevertheless, in a future 3D optimization project the problem can be tackled with a more effective space parallelization and a geometry and mesh allowing a larger timestep whilst fulfilling the CFL condition.

7. Contact Author Email Address

Corresponding author: Alessandro Porcarelli, now at Delft University of Technology, Faculty of Aerospace Engineering, Delft, Netherlands. Mailto: a.porcarelli@tudelft.nl.

8. Copyright Statement

The authors confirm that they, and/or their company or organization, hold copyright on all of the original material included in this paper. The authors also confirm that they have obtained permission, from the copyright holder of any third party material included in this paper, to publish it as part of their paper. The authors confirm that they give permission, or have obtained permission from the copyright holder of this paper, for the publication and distribution of this paper as part of the ICAS proceedings or as individual off-prints from the proceedings.

Acknowledgements

The author would like to thank Dr. Raffaello Mariani for providing feedback on the draft of this paper, and supervision during the master thesis work. The author would also like to thank Dr. Matteo Montecchia for help with the code in OpenFOAM and Francesco Fico for the inspiring discussions on the influence of the gravity term on the solution.

References

- [1] Lapeña-Rey N, Blanco JA, Ferreyra E, Lemus JL, Pereira S and Serrot E. A fuel cell powered unmanned aerial vehicle for low altitude surveillance missions. *International Journal of Hydrogen Energy*, Vol. 42, No. 10, pp 6926-6940, 2017.
- [2] Herwerth C, Chiang C, Ko A, Matsuyama S, Choi SB, Mirmirani M, ... and Jin P. Development of a small long endurance hybrid PEM fuel cell powered UAV *SAE Technical Paper*, No. 2007-01-3930, 2007.
- [3] Chiang C, Herwerth C, Mirmirani M, Ko A, Matsuyama S, Choi SB, ... and Jin P. Systems integration of a hybrid PEM fuel cell/battery powered endurance UAV. *46th AIAA Aerospace Sciences Meeting and Exhibit*, Reno, Nevada., p. 151, 2008.
- [4] Kim K, Kim T, Lee K and Kwon S. Fuel cell system with sodium borohydride as hydrogen source for unmanned aerial vehicles. *Journal of power sources*, Vol. 196, No. 21, pp 9069-9075, 2011.
- [5] Kim T and Kwon S. Design and development of a fuel cell-powered small unmanned aircraft. *International Journal of Hydrogen Energy*, Vol. 37, No. 1, pp 615-622, 2012.
- [6] Panagiotou P, Kaparos P, Salpingidou C and Yakinthos K Aerodynamic design of a MALE UAV. *Aerospace Science and Technology*, Vol. 50, pp 127-138, 2016.
- [7] Suetawanakul S, Porcarelli A, Olsson A, Grimler H, Chiche A, Mariani R and Lindbergh G. Conceptual design of a hybrid hydrogen fuel cell/battery blended-wing-body unmanned aerial aehicle — an overview. *Aerospace*, Vol. 9, No. 5, pp 275, 2022.
- [8] Porcarelli A. Development of a CFD model and methodology for the internal flow simulation in a hydrogen-powered UAV. <https://www.diva-portal.org/smash/record.jsf?pid=diva2%3A1599586&dswid=2306>, Master thesis, 2021.
- [9] Menter FR, and Kuntz M and Langtry R. Ten years of industrial experience with the SST turbulence model. *Turbulence, heat and mass transfer*, Vol. 4, No. 1, pp 625-632, 2003.
- [10] Eleni DC, Athanasios TI and Dionissios MP. Evaluation of the turbulence models for the simulation of the flow over a National Advisory Committee for Aeronautics (NACA) 0012 airfoil. *Journal of Mechanical Engineering Research*, Vol. 4, No. 3, pp 100-111, 2012.
- [11] Cadence Design Systems. Pointwise® V18.4R4. <https://www.pointwise.com>.
- [12] Weller HG, Tabor G, Jasak H and Fureby C. A tensorial approach to computational continuum mechanics using object-oriented techniques. *Computers in physics*, Vol. 12, No. 6, pp 620-631, 1998.
- [13] Issa RI. Solution of the implicitly discretised fluid flow equations by operator-splitting. *Journal of computational physics*, Vol. 62, No. 1, pp 40-65, 1986.
- [14] Vuorinen V, Keskinen JP, Duwig C and Boersma BJ. On the implementation of low-dissipative Runge–Kutta projection methods for time dependent flows using OpenFOAM® *Computers & Fluids*, Vol. 96, pp 153-163, 2014.
- [15] OpenFOAM contributors. Divergence scheme examples. <https://www.openfoam.com/documentation/guides/latest/doc/guide-schemes-divergence-example.html>, 2021.

- [16] Horizon – fuel cell technologies. H-1000 Fuel Cell Stack, user manual. https://2fca7bd6-9a97-4678-bc9f-28d3354f6ea2.filesusr.com/ugd/047f54_86b712599dda8542adcca251d9904ca4.pdf. 2013.
- [17] Ferziger JH and Perić M and Street RL. Computational methods for fluid dynamics. Springer. Vol. 3, 2002.